

Numerical investigation of controlling interfacial instabilities in non-standard Hele-Shaw configurations

Liam C. Morrow^{*}, Timothy J. Moroney^{*}, and Scott W. McCue^{*†}

Abstract

Viscous fingering experiments in Hele-Shaw cells lead to striking pattern formations which have been the subject of intense focus among the physics and applied mathematics community for many years. In recent times, much attention has been devoted to devising strategies for controlling such patterns and minimising the growth of the interfacial fingers. We continue this research by reporting on numerical simulations, based on the level set method, of a generalised Hele-Shaw model for which the geometry of the Hele-Shaw cell is altered. In particular, we investigate how imposing time-dependent injection rates and/or tapering the gap between the Hele-Shaw plates can be used to minimise the development of viscous fingering when an inviscid fluid is injected into a viscous fluid over a finite time period. Our results suggest that imposing these modifications can significantly suppress the growth of interfacial instabilities compared to the standard configuration for which the plates are parallel. Further, we illustrate how the number of non-splitting fingers can be controlled by injecting the inviscid fluid at a time-dependent rate while the gap between the plates is increased. While these non-standard configurations have been studied mathematically using linear stability analysis, our numerical scheme is able to accurately describe the full nonlinear dynamics of the problem. Our simulations compare well with previous experimental results for various injection rates and geometric configurations.

1 Introduction

A standard Hele-Shaw cell is an experimental device (figure 1) consisting of two parallel plates separated by a small gap filled with a viscous fluid. Fluid flow in this device has received significant attention largely due to the interfacial patterns that form when an inviscid fluid is injected into the viscous fluid. These viscous fingering patterns form due to the Saffman-Taylor instability [43], and are characterised by their distinctive branching and tip-splitting behaviour. Closely related interfacial instabilities appear in a wide variety of phenomena, including saturated flow in porous media [21], the growth of bacterial colonies [6], the crystal solidification [34], and fractal growth due to diffusion limited aggregation [46] amongst others, and the Hele-Shaw framework is often used as a model to describe these processes [5, 27, 25, 32].

In practice, the presence of fingering instabilities may be unwanted, for example in the application of oil recovery. As such, there is a significant body of research devoted to devising strategies for controlling the pattern formation and/or suppressing the viscous fingering [42]. The majority of these studies consider injecting the inviscid fluid at a time-dependent flow rate, while in recent times researchers have proposed to alter the geometry of the Hele-Shaw cell to affect the fingering pattern. Examples of such alterations include separating the plates in a time-dependent fashion [47], tapering the Hele-Shaw plates so that they are no longer parallel [3, 2, 7, 17, 23, 31, 45], and replacing one of the plates with an elastic membrane [1, 30, 41, 39, 40]. In the present study, we shall report on

^{*}School of Mathematical Sciences, Queensland University of Technology, Brisbane 4001, AUSTRALIA

[†]Corresponding author, Scott McCue, scott.mccue@qut.edu.au

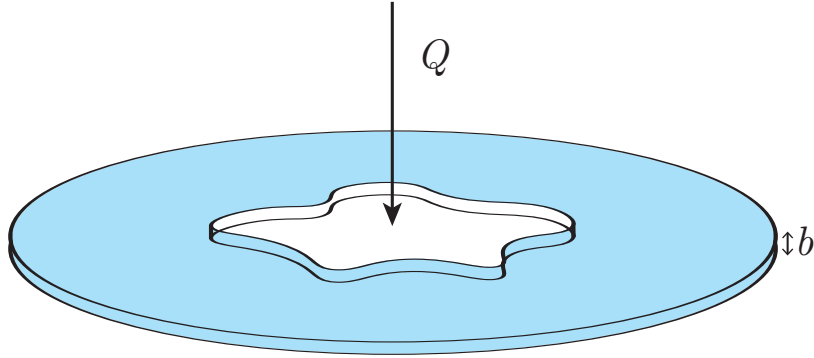


Figure 1: Illustration of the standard Hele-Shaw cell experiment with two parallel plates separated by a small gap filled with viscous fluid (shaded). An inviscid fluid (white) is injected into the viscous fluid at a rate Q . The immiscible fluids are separated by a sharp interface $\partial\Omega$, which becomes increasingly unstable as it expands, forming distinct viscous fingering patterns characterised by their branching and tip-splitting morphology.

fully nonlinear simulations of scenarios which combine some of these non-standard configurations, computed using a numerical scheme based on the level set method.

We have in mind two broad strategies for controlling viscous fingering instabilities in a Hele-Shaw experiment. The first involves injecting a prescribed amount of inviscid fluid over finite period of time, while minimising the development of the fingering pattern. For a standard Hele-Shaw cell with parallel plates, linear [15], piecewise [18] and sinusoidal [29] injection rates have been predicted to suppress the growth rate of the instabilities in comparison to the equivalent constant injection rate. We shall revisit this line of enquiry by allowing the plates to be tapered as in Al-Housseiny and Stone [2] and Bongrand and Tsai [7]. The second broad control strategy with which we shall be concerned involves adjusting the flow rate and the geometry of the experimental apparatus in an attempt to prevent ongoing tip splitting so that the pattern evolves with a predetermined number of fingers. For example, numerical, weakly nonlinear and experimental studies indicate that for a standard Hele-Shaw cell, an injection rate with the scaling $Q \sim t^{-1/3}$ can produce N -fold symmetric bubbles whose shape is independent of the initial condition, and can be controlled by the strength of the injection rate [8, 16, 25, 26]. Analogous results are suggested in the study of Zheng et al. [47], who apply linear stability analysis and experimental results to provide evidence that a constant number of fingers should develop if the parallel plates are separated via the scaling $b \sim t^{1/7}$. Again, we shall revisit these ideas using our fully nonlinear simulations.

The majority of mathematical studies concerned with the viscous fingering in non-standard Hele-Shaw geometry are performed using linear stability analysis. While linear stability analysis provides a valuable tool for studying nonlinear problems, its relevance is restricted to sufficiently small times such that the interface is near circular and nonlinear effects are negligible. Thus, we must resort to numerical techniques to study the long term behaviour of the solutions. Typically, numerical solutions to the standard Hele-Shaw problem are found using the boundary integral method, which requires that the pressure of the viscous fluid to be harmonic [13, 14, 26, 44]. However, in general this is no longer true when the gap between the plates becomes a function of time and/or space, and thus more flexible schemes are required. As such, we shall employ a robust numerical scheme based on the level set method, presented in Appendix A. This scheme is capable of describing the complex interfacial patterns which develop in the Hele-Shaw cell, and produces solutions consistent with experimental results. From these simulations, we provide insight into how altering the time-dependent injection rate and the physical geometry of a Hele-Shaw cell influence the evolution of the inviscid-viscous fluid interface which extend well beyond the limitations of linear stability analysis.

The outline of this paper is as follows. In §2, we summarise a generalised model for Hele-Shaw flow in a non-standard geometry, for which the gap between the plates depends on both time and

space. In §3, we compare numerical simulations for the standard Hele-Shaw configuration (parallel stationary plates with constant injection rate) with experimental results and predictions from linear stability analysis. We show that the numerical simulations agree with predictions from linear stability analysis for small time, and reproduce key morphological observed in experiments for large time. In §4, we consider the control strategy of injecting a prescribed amount of fluid over fixed period of time, and present numerical results indicating that both tapering the gap between the plates and/or implementing a time-dependent injection rate can be used to reduce the growth of interfacial instabilities. Subsequently, in §5, we treat the control strategy of preventing tip-splitting and show that careful implementation of a time-dependent gap and/or injection rate can control the number of viscous fingers that develop. Finally, in §6 we conclude by discussing the results and suggesting possibilities for future work.

2 Mathematical model

2.1 Governing equations

The geometry we have in mind involves the injection of an incompressible inviscid fluid (with flow rate Q) through a small orifice in the centre of a Hele-Shaw cell otherwise filled with a viscous fluid (figure 1). We assume the two fluids are immiscible and denote the simply connected domain of inviscid fluid by $\Omega(t)$ and the interface between the two fluids by $\partial\Omega$. In our model, the viscous fluid is infinite in its extent, and so while the problem is driven by injection of an inviscid fluid at a point, we can also interpret the flow as being driven by a suction of viscous fluid from infinity. A feature of our model is that we allow the small gap between the plates, b , to depend on both space and time.

We use a two-dimensional model of Hele-Shaw flow that is derived by averaging Stokes flow over the small gap between the plates. Denoting p , \mathbf{q} and μ as the pressure, velocity and viscosity of the viscous fluid, the governing field equations are

$$\mathbf{q} = -\frac{b^2}{12\mu}\nabla p, \quad \mathbf{x} \in \mathbb{R}^2 \setminus \Omega(t), \quad (1)$$

$$\nabla \cdot (b\mathbf{q}) = -\frac{\partial b}{\partial t}. \quad \mathbf{x} \in \mathbb{R}^2 \setminus \Omega(t), \quad (2)$$

Equation (1) is analogous to Darcy's law, which provides an intimate connection between Hele-Shaw flow and porous media flow [21]. Equation (2) ensures that the fluid's volume is conserved, and reduces to the traditional divergence free condition, $\nabla \cdot \mathbf{q} = 0$, in the standard configuration for which the plates are parallel and stationary. Note that we shall ignore the pressure gradients in the inviscid domain $\Omega(t)$, which makes this a one-phase Hele-Shaw model.

By substituting (1) into (2), we have the Reynolds lubrication equation

$$\nabla \cdot \left(\frac{b^3}{12\mu} \nabla p \right) = \frac{\partial b}{\partial t} \quad \mathbf{x} \in \mathbb{R}^2 \setminus \Omega(t). \quad (3)$$

The boundary conditions on the interface are

$$p = -\sigma \left(\kappa + \frac{2}{b} \right) \quad \mathbf{x} = \partial\Omega(t), \quad (4)$$

$$v_n = -\frac{b^2}{12\mu} \frac{\partial p}{\partial n} \quad \mathbf{x} = \partial\Omega(t). \quad (5)$$

The dynamic boundary condition (4) incorporates the effects of surface tension, where σ is the surface tension parameter and κ is the signed curvature of the interface in the lateral direction. The term $2/b$ in (4) represents the curvature in the transverse direction for the case where the fluid is perfectly wetting [42]. The kinematic boundary condition (5) equates the velocity of the interface to the velocity of the viscous fluid on the interface. We note that both viscous stresses and the effect

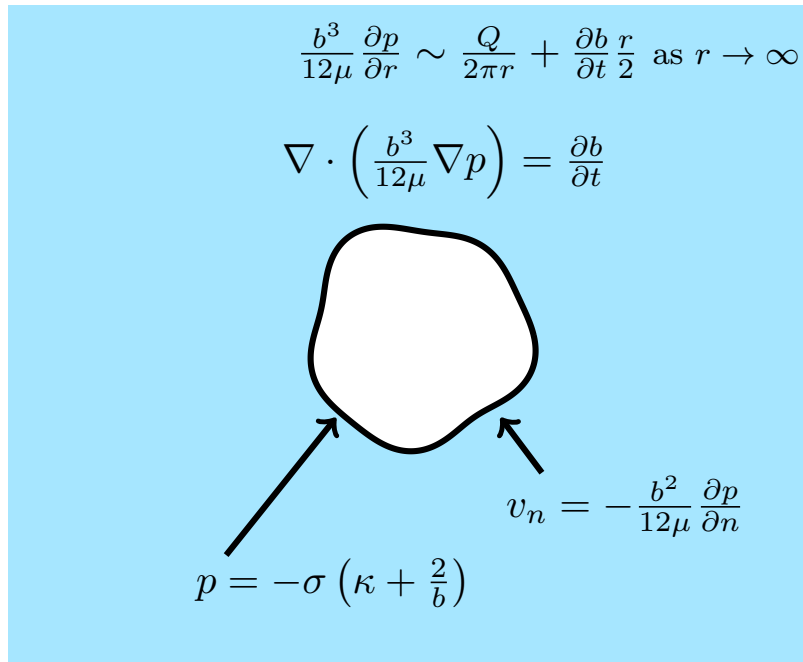


Figure 2: A schematic of our generalised Hele-Shaw model with spatially and/or temporally dependent plate gap thickness (1)-(6). The viscous fluid is represented by the shaded (blue) region, and the inviscid bubble is represented by the white region.

of a thin wetting film left behind by the viscous fluid are ignored. The far-field boundary condition is

$$\frac{b^3}{12\mu} \frac{\partial p}{\partial r} \sim \frac{Q}{2\pi r} + \frac{\partial b}{\partial t} \frac{r}{2} \quad r \rightarrow \infty, \quad (6)$$

where Q is a time-dependent flow-rate at which the inviscid fluid is injected. Our model is summarised by a schematic in figure 2.

We note in passing that the complementary problem with viscous fluid in $\Omega(t)$ and inviscid fluid in $\mathbb{R}^2 \setminus \Omega(t)$ has attracted interest in the literature. For that scenario, the lifting-plate configuration causes fingers to develop inwards. This problem has been studied through a combination of experimental, analytical, and numerical techniques [9, 16, 28, 35, 44], but will not be pursued here.

2.2 Numerical scheme

Many numerical schemes used to study viscous fingering in a standard Hele-Shaw cell, where the governing equation for pressure (3) reduces to Laplace's equation $\nabla^2 p = 0$, implement a boundary integral method [13, 14, 26, 44]. However, for non-standard Hele-Shaw configurations, i.e. when the gap between the plates is spatially and/or temporally dependent, the pressure is no longer harmonic and boundary integral methods become a less desirable option. For our study, we utilise the level set method, proposed by [36], which is based around the idea of representing interfaces implicitly as the zero level set of a higher dimensional hypersurface. We note that other flexible numerical schemes based on front tracking methods have been used to study viscous fingering in non-standard Hele-Shaw cells [20, 39]. One advantage of the level set method is that it can be used describe the evolution of complex interfacial patterns using a uniform grid, eliminating the need to generate meshes that adapt as the interface evolves. The level set method has previously been used to study interfacial instabilities in a variety of moving boundary problems, including Hele-Shaw flow [22, 29] and Stefan problems [11]. We summarise the details of our scheme in Appendix A.

3 Review of standard configuration

Most mathematical studies investigating the influence of manipulating the geometry of the Hele-Shaw cell on viscous fingering are performed using linear stability analysis. While this approach provides a useful tool for understanding the qualitative behaviour of solutions, as well as for deriving strategies for controlling viscous finger development, it is only accurate for small time and, as such, does not capture the full nonlinear dynamics of the problem. In this section, we review linear stability analysis for the standard Hele-Shaw problem where the plates are parallel and stationary (b constant) and the inviscid fluid is injected at a constant rate Q . Further, we show that our numerical simulations are consistent with predictions made by linear stability analysis when time is sufficiently small, and can accurately reproduce experimental results for longer times.

Considering (1)-(6) in polar coordinates (r, θ) with $p = p(r, \theta, t)$ and the interface $\partial\Omega$ denoted by $r = s(\theta, t)$, we assume a perturbed circular solution

$$p(r, \theta, t) = p_0(r, t) + \varepsilon P_n(t) r^{-n} \cos n\theta + \mathcal{O}(\varepsilon^2), \quad (7)$$

$$s(\theta, t) = s_0(t) + \varepsilon \gamma_n(t) \cos n\theta + \mathcal{O}(\varepsilon^2), \quad (8)$$

where $\varepsilon \ll 1$ and $n \geq 2$. The leading order radius of the interface can be solved for to give $s_0 = \sqrt{s_0(0) + Qt/\pi b}$. The resulting differential equation for the n th mode of perturbation is [37]

$$\frac{\dot{\gamma}_n}{\gamma_n} = \frac{n-1}{s_0} \left(\frac{Q}{2\pi b s_0} - \frac{n(n+1)b^2\sigma}{12\mu s_0^2} \right), \quad (9)$$

where the most unstable mode of perturbation, n_{\max} , is

$$n_{\max} = \sqrt{\frac{1}{3} \left(1 + \frac{6\mu Q s_0}{\pi\sigma b^3} \right)}. \quad (10)$$

Equation (10) comes from setting $\partial(\dot{\gamma}_n/\gamma_n)/\partial n = 0$ and solving for n . As such, n_{\max} is not an integral, and so in practice the most unstable mode is the closest integer to n_{\max} . Note that, given s_0 is an increasing function of time, then n_{\max} also increases in time, which means the most unstable mode predicted by linear stability is a dynamic property (while not strictly relevant for fully nonlinear pattern formation, this observation is closely related to the ongoing tip-splitting that occurs in for longer times).

We compare predictions made by this linear stability analysis with experimental results performed by [10] and numerical simulations, shown in figure 3. This figure illustrates the classic pattern formation in a standard Hele-Shaw configuration for three different injection rates in decreasing order (noting that in each case, the same amount of fluid is injected into the cell). For early times, we can apply (10) to predict the number of fingers that are produced. Using figure 3(e) as an example, equation (10) (with the appropriate parameter values) predicts that $n_{\max} \approx 9$ for small times, suggesting that 9 fingers should initially form. A manual count of the small ‘‘fingers’’ in 3(e) shows this prediction is consistent with the numerical simulation.

Another straightforward result from (9) is that, for fixed σ , b and μ , increasing the flow rate Q results in a positive contribution to $\dot{\gamma}_n/\gamma_n$, which has a destabilising effect on each mode. Further, we see from (10) that increasing Q has the effect of increasing the rate at which the most unstable mode increase. These observations are consistent with the experimental measurements performed by [10] (and many others), which appear to show that increasing the injection rate results in larger wave numbers becoming more unstable, leading to branching and tip-splitting. Of course, for later times, nonlinear effects become significant and linear stability analysis no longer provides an accurate description of the solution. In this nonlinear regime, our numerical simulations are able to reproduce the main morphological features of these experiments for the different injection rates considered, as we can see by comparing images in each column of figure 3. We view this comparison as a preliminary test of our numerical method.

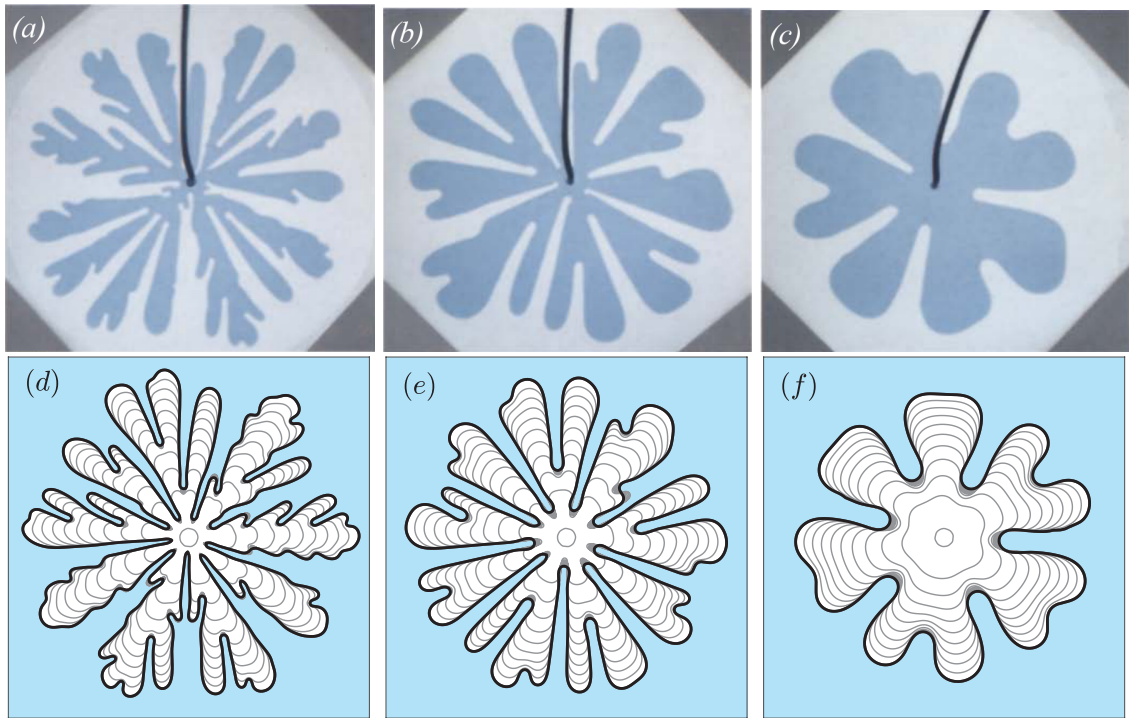


Figure 3: (a-c) Experimental results from [10], reproduced with permission, comparing the development of viscous fingers for different injection rates and (d-f) the corresponding numerical simulations. The gap thickness between plates is 7.5×10^{-3} cm, and the injection rate and final times (left to right) are: $Q = 2 \times 10^{-3}$ mL/s and $t_f = 65$ s; $Q = 4.5 \times 10^{-4}$ mL/s and $t_f = 490$ s; and $Q = 1.4 \times 10^{-4}$ mL/s and $t_f = 1650$ s. Numerical solutions are plotted in time intervals of $t_f/10$.

4 Minimising growth of viscous fingering pattern

In this section, we investigate strategies for controlling viscous fingering when a prescribed amount of the inviscid fluid is injected over a finite period of time. To begin, we consider whether imposing a time-dependent injection rate and/or linearly tapering the gap between plates can be used to suppress the development of viscous fingers. While these strategies have been studied previously using linear stability analysis, we extend this work by performing fully nonlinear numerical simulations to better understand the effectiveness of these strategies.

We consider two metrics for measuring how severe a fingering pattern is at the interface, namely the isoperimetric ratio

$$\mathcal{I}(t) = \frac{L^2}{4\pi A}, \quad (11)$$

where L and A are the arc length and area of the interface, and the ratio of the tip to base radii, which we refer to as the circularity ratio, defined as

$$\mathcal{C}(t) = \frac{\max(s(\theta, t))}{\min(s(\theta, t))}. \quad (12)$$

Both \mathcal{I} and \mathcal{C} will be unity when the interface is circular and increase as the instabilities cause the interface to deform away from a circle. In this section, the initial condition of the interface is

$$s(\theta, 0) = R_0 \left(1 + 0.01 \sum_{n=2}^{12} \cos(n(\theta - 2\pi\theta_0)) \right),$$

where θ_0 is a uniformly random number between 0 and 1. For each parameter combination considered, 10 simulations are performed, and \mathcal{I} and \mathcal{C} are averaged over these simulations.

4.1 Time-dependent injection rate

The first strategy we consider is proposed by [15], who, using linear stability analysis and optimal control theory, derived a time-dependent injection rate when the plate gap thickness is uniform. By seeking solutions of the form of (7) and (8), Dias *et al.* showed that the growth rate of perturbations to the circular solution, s_0 , when the inviscid fluid is injected over the time interval $0 \leq t \leq t_f$ are minimised when

$$Q(t) = 2\pi b \frac{R_f - R_0}{t_f} \left(R_0 + \frac{R_f - R_0}{t_f} t \right), \quad (13)$$

where $s_0(0) = R_0$ and $s_0(t_f) = R_f$. The average of (13) over this time period is

$$\bar{Q} = \pi b \frac{R_f^2 - R_0^2}{t_f}.$$

We are interested in comparing results from the linear injection rate (13) with a constant injection rate where $Q = \bar{Q}$, so that in both cases the same amount of fluid is injected over the fixed time period. Figure 4 presents numerical solutions for the constant (top row) and linear (second row) injection rates. The columns from left to right are for increasing values of \bar{Q} . We observe that the linear injection rate appears to inhibit viscous fingering, and in particular, tip-splitting is delayed resulting in shorter fingers than the corresponding constant injection case.

These are only visual observations. Focusing on the representative case $\bar{Q} = 1.6$ mL/s (third column of figure 4), a more quantitative measure is provided in figure 5(a), where the isoperimetric ratio \mathcal{I} is plotted against time for both injection schemes. Initially, the isoperimetric ratio of the linear injection rate case (second curve from top in figure 5(a)) grows much more slowly than the constant injection rate case (top curve), which is simply because the linear injection rate is initially lower than the constant injection rate, and so the interface is less unstable. For later times, the

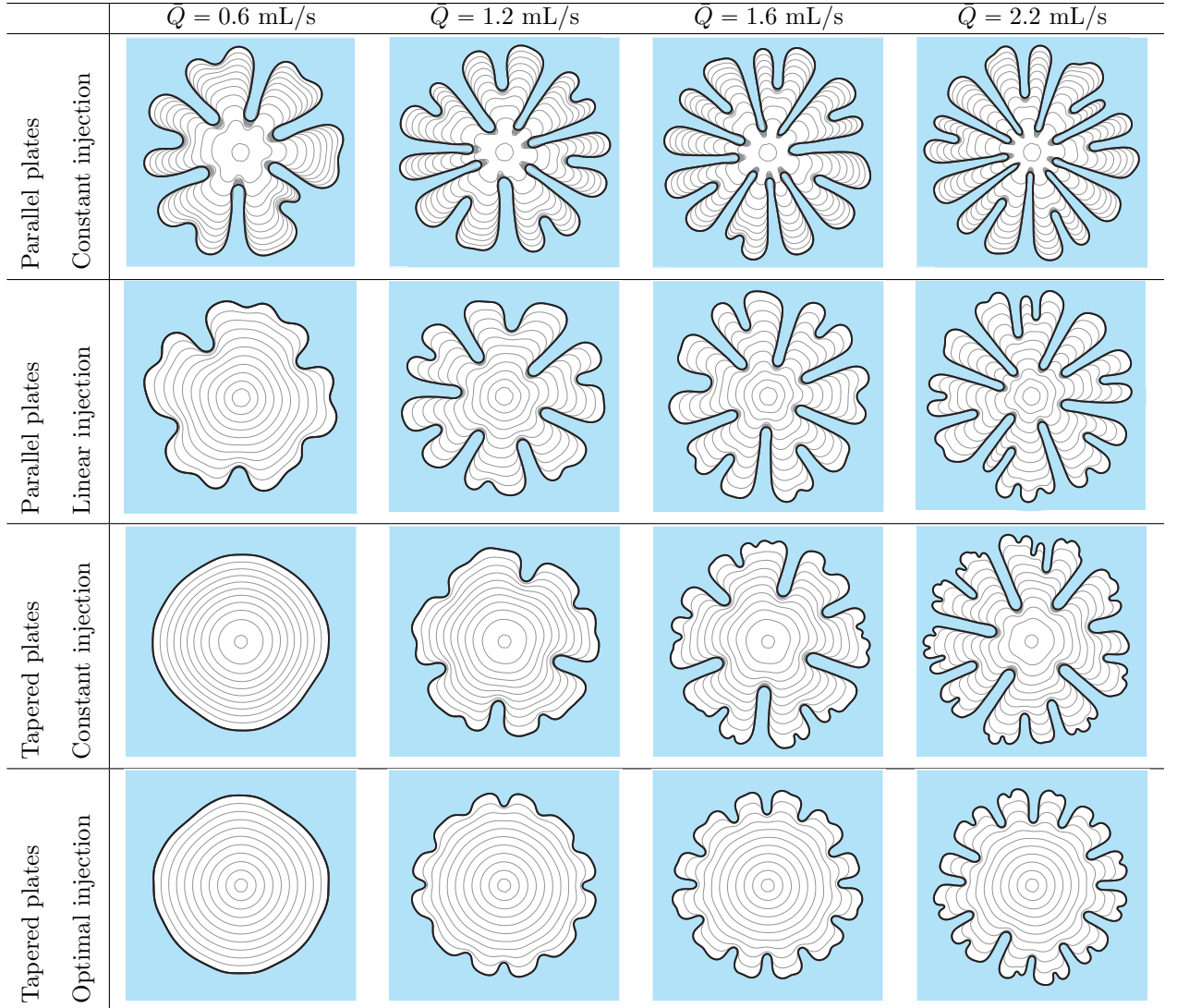


Figure 4: Comparison of numerical simulations with different injection schemes and plate gap taperings. The parameter \bar{Q} (mL/s) is the average injection rate over the duration of a simulation. For a particular column, the same amount of inviscid fluid is injected over the same time period, which is (left to right) $t_f = 25.62$ s, 12.81 s, 9.61 s, and 6.99 s. First row is interface profiles with parallel plates such that $b = 0.2$ cm with constant injection rate, \bar{Q} mL/s. Second row is constant gap thickness $b = 0.2$ cm and linearly increasing injection rate (13) with $R_0 = 0.5$ and $R_f = 5$. Third row is constant injection rate with tapered plates of the form of (14) with $r_0 = 7$ cm, $b_0 = 5 \times 10^{-3}$ cm, and $\alpha = 5.3 \times 10^{-2}$. Fourth row is time-dependent injection rate computed from the solution to (19) with $R_0 = 0.37$ and $R_f = 5$, where the gap between plates is the same as row three. Profiles are plotted in time intervals of $t_f/10$. For all simulations, the initial volume of the bubble is approximately 0.157 mL, and the volume at $t = t_f$ is 15.7 mL.

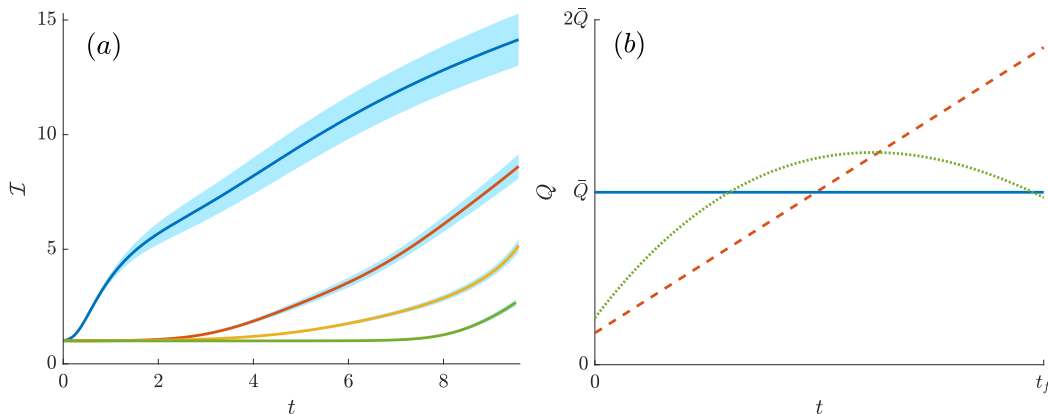


Figure 5: (a) Isoperimetric ratio for different injection schemes and plate tapering configurations, all with the same average injection rate $\bar{Q} = 1.6$ mL/s and the final time $t_f = 9.605$ s. From top to bottom, the solid curves denote configurations with: (blue) gap thickness $b = 0.2$ cm and constant injection rate; (red) $b = 0.2$ cm and linear injection rate (13) with $R_0 = 0.5$ and $R_f = 5$; (yellow) tapered plates of the form (14) with $b_0 = 5 \times 10^{-3}$ cm, $r_0 = 7$ cm, and $\alpha = 5.3 \times 10^{-2}$ with constant injection; and (green) tapered plates of the form (14) with $b_0 = 5 \times 10^{-3}$ cm, $r_0 = 7$ cm, and $\alpha = 5.3 \times 10^{-2}$, with injection rate computed from solution to (19) with $R_0 = 0.37$ and $R_f = 5$. In all cases, the shaded region represents one standard deviation above and below the mean. (b) Sketch of different injection rates as a function of time. Solid line (blue) is constant injection rate, dashed line (red) is optimal injection rate for parallel plates, and dotted line (green) is optimal injection rate for the tapered plate configuration ($\alpha > 0$). The total amount of inviscid fluid injection over the time intervals $[0, t_f]$ is the same for all injection rates.

isoperimetric ratio of the linear injection rate case grows faster corresponding to times for which the linear injection rate is faster. Despite this switch in behaviour, the overall effect of the linear injection rate (13) is to greatly reduce the isoperimetric ratio at the final time t_f when compared to the constant injection rate. These numerical results provide new quantitative evidence for how well [15]’s ‘optimal’ flow rate works in practice.

To investigate the robustness of the linear injection strategy as \bar{Q} is varied, we compute both the isoperimetric and circularity radii ratios according to (11) and (12) at $t = t_f$ for both the constant and linear injection rates, shown in figure 6. The results for the constant injection rates are denoted by the (blue) upward triangle, while the linear injection rate is indicated by the (red) downward triangles. Recall that for each data point, 10 simulations are performed and the error bars indicate plus or minus one standard deviation. Over the range of \bar{Q} values considered, both of the measures \mathcal{I} and \mathcal{C} are considerably lower for the linear injection rate case compared to the constant injection rate. Thus we conclude the linear injection scheme is successful in greatly reducing the fingering pattern, regardless of \bar{Q} .

4.2 Tapered Hele-Shaw geometry

We consider the configuration where the inviscid fluid is injected at a constant rate and the gap between the plates is linearly tapered in the direction of the flow such that

$$b(r) = b_0 - \alpha(r - r_0). \quad (14)$$

The parameter α controls the gradient of the taper such that $\alpha = (b(0) - b_0)/r_0$. The influence of tapering the plates of a Hele-Shaw cell has been studied using linear stability analysis in both channel and radial geometry [3, 2]. By considering $\alpha \ll 1$, [2] were able to derive an ordinary differential equation for γ_n

$$\frac{\dot{\gamma}_n}{\gamma_n} = \frac{n-1}{s_0} \left(\dot{s}_0 - \frac{n(n+1)b^2}{12\mu s_0^2} \sigma \right) - \left(\frac{n\sigma}{6\mu s_0} - \frac{\dot{s}_0}{b} \right) \alpha, \quad (15)$$

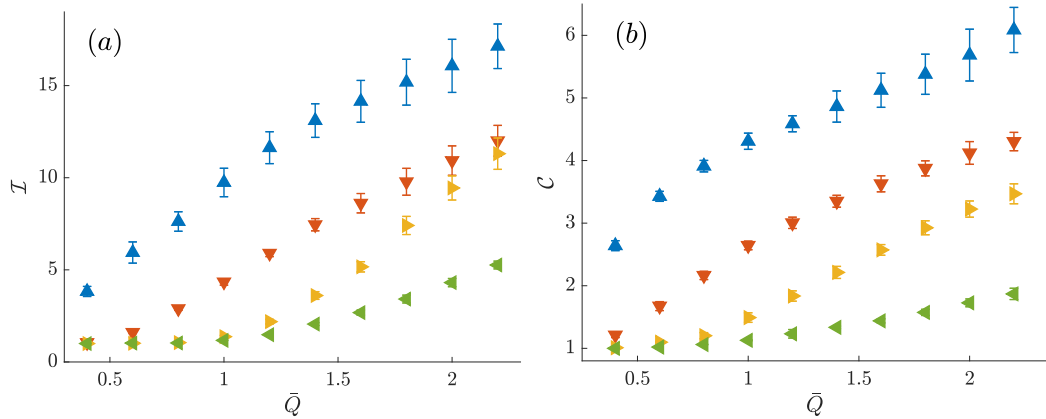


Figure 6: (a) Isoperimetric (11) and (b) circularity (12) ratios at the final time $t = t_f$ for different injection schemes and plate tapering. The parameter \bar{Q} (mL/s) is the average injection rate over a simulation, and the final time is $t_f = 99\pi/20\bar{Q}$ s. Upward (\blacktriangle , blue) and downward (\blacktriangledown , red) facing triangles denote the standard configuration with parallel plates $b = 0.2$ cm, while left (\blacktriangleleft , yellow) and right (\blacktriangleright , green) facing triangles denote the case where the plates are tapered as in (14) with $b_0 = 5 \times 10^{-3}$ cm, $r_0 = 7$ cm, and $\alpha = 5.3 \times 10^{-2}$. For \blacktriangle and \blacktriangleright , the inviscid fluid is injected at a constant rate, \bar{Q} . For \blacktriangledown , injection rate is (13) with $R_0 = 0.5$ and $R_f = 5$. For \blacktriangleleft , the injection rate is computed from the solution to (19) with $R_0 = 0.37$ and $R_f = 5$.

where $\dot{s}_0 = Q/2\pi b(s_0)s_0$, which suggests the most unstable mode of perturbation is

$$n_{\max} = \sqrt{\frac{1}{3} + \frac{4\mu s_0^2 \dot{s}_0}{b^2 \sigma} - \frac{2s_0^2 \alpha}{3b}}. \quad (16)$$

Of course, by setting $\alpha = 0$, (15) and (16) reduce to (9) and (10). When injecting the inviscid fluid at a constant rate, we can infer from (15) and (16) that tapering the plates in a converging configuration acts to slow the growth of the most unstable mode of perturbation compared to the corresponding parallel plate case (this behaviour is analogous to the time-dependent injection rate considered in §4.1).

The tapered Hele-Shaw problem is considered experimentally by [7], who investigate the effect of α , b_0 , and Q on the development of instabilities. In particular, Bongrand and Tsai show that for a particular value of α , there exists a critical injection rate, Q_c , such that for $Q < Q_c$, the interface remains stable over the duration of the experiment. To demonstrate that our numerical solutions of (1)-(6) are consistent with the experimental results of [7], we compare simulations with these experiments for different values of α , b_0 , and Q , shown in figure 7. When the plates are parallel, $\alpha = 0$, our simulations are able to reproduce the classic viscous fingering patterns observed experimentally. When the plates are converging ($\alpha > 0$) and the injection rate is sufficiently low, experimentally it is observed that the interface is stabilised, which is what we see with our numerical simulations. For a faster injection rate, the interface is unstable and develops fingers that appear slightly different to traditional viscous fingers (although the mechanism is essentially the same), and our numerical solution is able to reproduce this morphology.

Returning to our control strategy which involves injecting the same volume of inviscid fluid over a fixed period of time, we compare numerical solutions in figure 4 for both $\alpha = 0$ and $\alpha > 0$ for four different constant injection rates. We see that tapering the plates in the direction of flow (third row of figure 4) delays tip-splitting and produces shorter fingers compared to the corresponding parallel plate configuration (first row of figure 4). Furthermore, for the lowest of the four injection rates, $\bar{Q} = 0.6$ mL/s (first column of figure 4), tapering the plates completely suppresses the development of viscous fingers over the duration of the simulation.

To better quantify how the interfacial instabilities develop when the plates are tapered over the duration of a simulation, we compare the isoperimetric ratio for the tapered and parallel plate

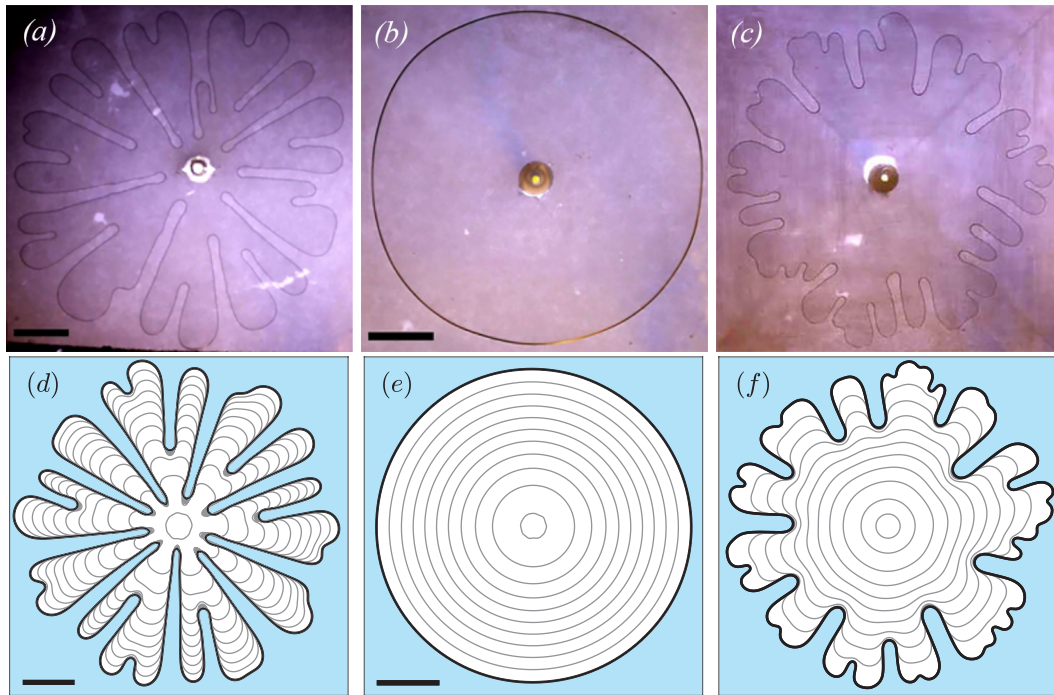


Figure 7: (a-c) Experimental results from [7], reproduced with permission, comparing the viscous fingering pattern for different injection rates and plate configurations, and (d-f) the corresponding numerical simulations. The gap thickness is of the form (14) with (d) $Q = 2/3$ mL/s, $b_0 = 0.12$ cm, $\alpha = 0$, and $t_f = 14$ s, (e) $Q = 2/3$ mL/s, $b_0 = 1.5 \times 10^{-2}$ cm, $\alpha = 6.67 \times 10^{-2}$, $r_0 = 7$ cm, and $t_f = 30$ s, and (f) $Q = 11/6$ mL/s, $b_0 = 5 \times 10^{-2}$ cm, $\alpha = 4.75 \times 10^{-2}$, $r_0 = 7$ cm, and $t_f = 4.5$ s. Black scale bars represent a length of 2 cm.

configurations for a particular flow rate, shown in figure 5(a). Initially, the isoperimetric ratio for the tapered configuration (right-facing triangles) grows much more slowly than the parallel plate configuration (upward-facing triangles), while for later times it increases at a faster rate. However, as with linear injection strategy discussed in §4.1, despite the increase in \mathcal{I} in the later stages of the simulation, tapering the plates results in an overall reduction of \mathcal{I} at the final time $t = t_f$ compared to the corresponding parallel plate configuration.

Both the isoperimetric \mathcal{I} and circularity \mathcal{C} ratios at $t = t_f$ are shown in figure 6 for various values of \bar{Q} . For all parameter combinations tested, tapering the plates (right-facing triangles) produces a much more circular interface than the parallel plate case (upward-facing triangles). A further comparison can be made between the tapered plate case (right-facing triangles) with the linear injection case of §4.1 (downward-facing triangles). Here, the general trend is that the measures \mathcal{I} and \mathcal{C} are lower for the former than the latter; however, figure 6(a) indicates that \mathcal{I} at $t = t_f$ may increase above the linear injection rate case for $\bar{Q} > 2.2$ mL/s. We discuss this issue further in §4.4.

4.3 Tapered plates with time-dependent injection

In §4.1 and §4.2, we demonstrate that employing either the linearly increasing injection rate (13) (in a parallel plate configuration), or tapering the gap between the plates according to (14) (with constant injection rate) results in a less unstable interface than the corresponding constant injection case with parallel plates. We now go further by, in the spirit of [15], deriving an optimal injection rate that minimises viscous fingering when the gap thickness is of the form of (14). We also perform numerical simulations to investigate the effectiveness of this configuration for minimising finger growth.

To derive the relevant optimal injection rate, we assume that $12\mu\dot{s}_0s_0^2/\sigma b^2 \gg 1$ such that the most unstable mode of perturbation can be approximated by

$$n_{\max} \approx \sqrt{\frac{4\mu\dot{s}_0s_0^2}{\sigma b^2}},$$

Furthermore, (15) evaluated at $n = n_{\max}$ reduces to

$$\frac{\dot{\gamma}_n}{\gamma_n} \approx \sqrt{\frac{4\mu}{\sigma b^2}} \dot{s}_0^{3/2} - \frac{\dot{s}_0}{s_0}. \quad (17)$$

As explained by [15], the optimal injection rate that minimises the growth of the most unstable perturbation can be determined from the solution to the Euler-Lagrange equation

$$\frac{d}{dt} \left(\frac{\partial}{\partial \dot{s}_0} \frac{\dot{\gamma}_n}{\gamma_n} \right) = \frac{\partial}{\partial s_0} \frac{\dot{\gamma}_n}{\gamma_n}. \quad (18)$$

By substituting (17) into (18), we arrive at the second order, nonlinear differential equation

$$3b\ddot{s}_0(t) + 2\alpha\dot{s}_0^2 = 0, \quad (19)$$

with boundary conditions $s_0(0) = R_0$ and $s_0(t_f) = R_f$. We note that when $\alpha = 0$, (19) reduces to $\ddot{s} = 0$, the same equation derived by [15]. While an explicit expression for $s_0(t)$ cannot be found, we can solve for (19) numerically and compute the optimal injection rate as $Q(t) = 2\pi\dot{s}_0s_0b$. The result of this computation is presented in figure 5(b), where we compare the optimal injection rate for the tapered and parallel plate cases. This figure illustrates that while both rates are initially slower than the corresponding constant rate, the optimal rate for $\alpha \neq 0$ does not monotonically increase. Instead it decreases such that ultimately it is slightly slower than the constant rate at $t = t_f$.

To illustrate the effect of implementing our new optimal injection rate when the plates are tapered, we include numerical results in the fourth row of figure 4. To ensure the comparison with the previous three configurations is fair, we ensure the solutions are computed for the same average flow rates (we use $\bar{Q} = 0.6, 1.2, 1.6$ and 2.2 mL/s in columns 1-4, respectively) over the same period of time. Imposing a time-dependent injection rate when the plates are tapered significantly changes

the morphology of the interface. Specifically, the interface appears to remain stable until near the end of the simulation, where numerous fingers form over the final time interval. It is interesting to note these fingers appear significantly shorter than the fingers which develop for the other configurations, as we discuss shortly.

For the representative case representative case $\bar{Q} = 1.6$ mL/s (third column of figure 4), the isoperimetric ratio is shown in figure 5(a). We see that when the plates are tapered and the injection rate is optimal, the interface remains almost circular for almost all of the simulation. For late times, the isoperimetric ratio sharply increases as the short fingers, observed in figure 5(a), begin to develop. Despite this increase, the isoperimetric ratio is smaller at $t = t_f$ compared to the other three configurations we have considered. In figure 6, we compare both the isoperimetric and circularity ratios computed at $t = t_f$ for all four configurations as a function of \bar{Q} . This figure shows that both \mathcal{I} and \mathcal{C} are reduced for the optimal injection/tapered plate configuration over the entire range of parameters investigated.

4.4 Discussion

In this section, we have considered several strategies for minimising viscous fingering when a fixed amount inviscid fluid is injected over a finite time interval. In particular, we investigate how imposing a time-dependent injection rate and/or tapering the plate gap influences the morphology of the interface. By performing a series of numerical simulations, we have shown that each of these configurations produces a less unstable interface at $t = t_f$ than the standard configuration with constant injection rate and parallel plates. In particular, our results indicate that injecting at a wisely chosen time-dependent rate when $\alpha > 0$ is the most effective configuration for minimising instabilities. Note that ours are the first fully numerical results for these three non-standard configurations.

It is interesting to note the different morphological features that are produced by the tapered plate configurations. For example, for the tapered case with constant injection rate (third row of 4), the interface remains circular for a longer time period compared to the parallel plate case with an optimal injection rate (second row of 4). However, when $t_f - t \ll 1$, the interface in the former case quickly develops numerous short fingers. This behaviour is consistent with the experimental results of [7], who observed that a stable interface can quickly become unstable when the plates are tapered. For larger values of \bar{Q} , this tip-splitting behaviour results in the isoperimetric ratio to sharply increase near the end of a simulation, but does not significantly influence the circularity ratio. These results are reflected in figure 6, which suggests for $\bar{Q} > 2.2$, \mathcal{I} at $t = t_f$ for the tapered configuration may increase above the parallel plate with time-dependent injection rate configuration, but \mathcal{C} will remain smaller. This behaviour is more apparent for the tapered plate with optimal injection rate configuration (fourth row of 4). In particular, numerical simulations show that the interface remains stable significantly longer than the other configurations considered. However, when $t_f - t \ll 1$, many short fingers develop over a short time period. We note that the shape of these fingers resemble the short ‘‘stubby’’ fingers observed both experimentally and numerically by [38, 41], who considered a Hele-Shaw cell where the top plate is replaced by an elastic membrane.

5 Controlling number of fingers

5.1 Lifting plates configuration

Numerous theoretical and experimental investigations have been performed to determine strategies for controlling the number of non-splitting fingers which develop in a Hele-Shaw cell. Using linear stability analysis, [47] proposed that if the gap thickness and injection rates are of the forms $b = b_1 t^{\alpha_b}$ and $Q = Q_1 t^{\alpha_Q}$ where $7\alpha_b - 3\alpha_Q = 1$, then the expected number of fingers is

$$N \approx \sqrt{\frac{1+J}{3}}, \quad (20)$$

where

$$J = \frac{6\mu Q_1^{3/2}}{\pi^{3/2}(\alpha_Q + 1)^{1/2} \sigma b_1^{7/2}},$$

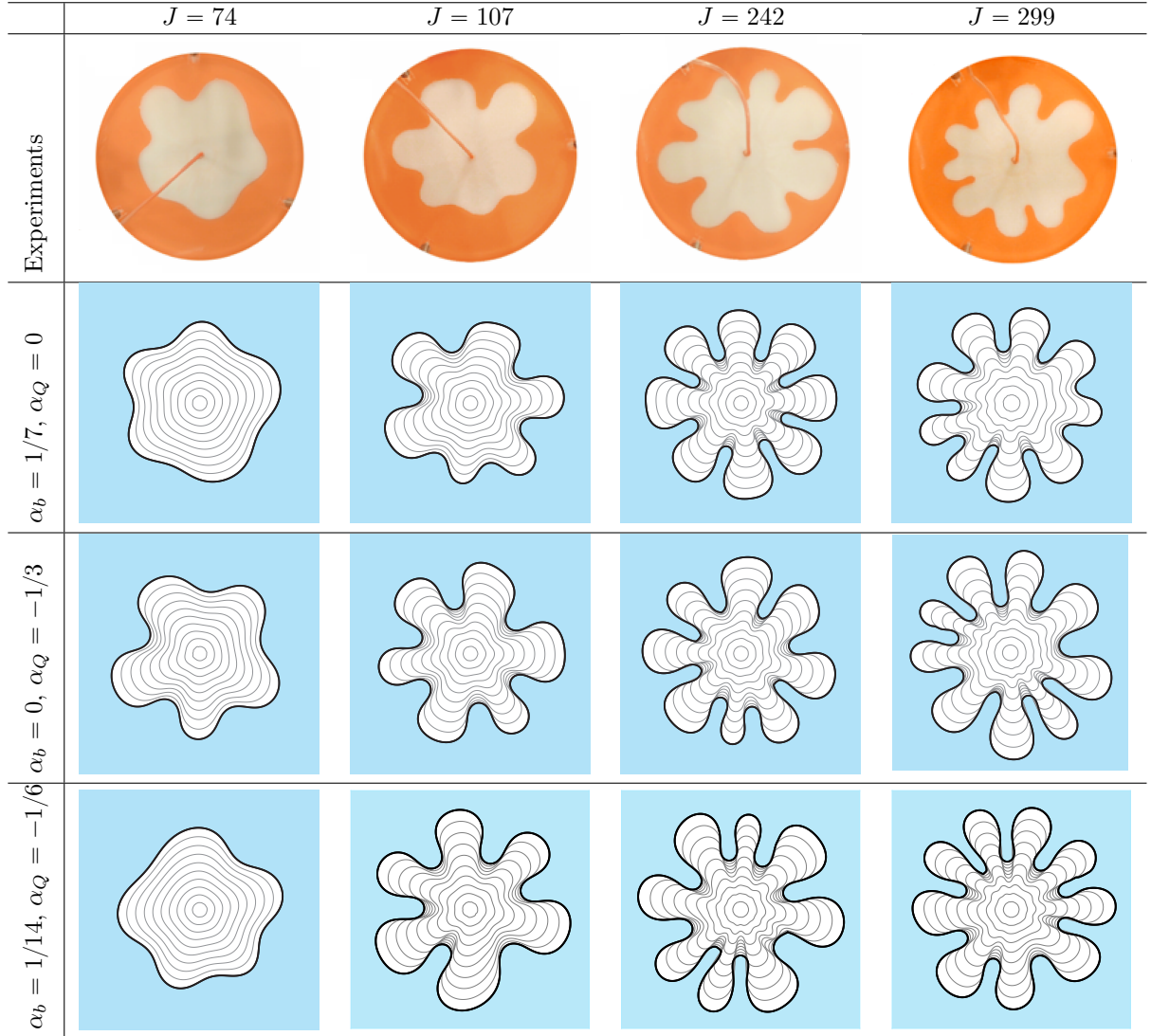


Figure 8: Top row shows experimental results from [47] where the plates are separated according to $b = b_1 t^{1/7}$, each produced for a different value of the control parameter J , reproduced with permission. Rows 2 to 4 are numerical simulations with distance between plates and injection rate of the form $Q = Q_1 t^{\alpha_Q}$ and $b = b_1 t^{\alpha_b}$ for different values of α_Q and α_b . For row 2, $Q = 1.2 t^{-1/3}$ mL/s, $b = 0.12$ cm and (left to right) $\sigma = 3.264, 2.257, 1,$ and 0.808 g/s². For row 3, $Q = 1.2$ mL/s, $b_1 = 0.205 t^{1/7}$ cm, and (left to right) $\sigma = 0.410, 0.284, 0.126,$ and 0.102 g/s². For row 4, $Q = 1.2 t^{-1/6}$ mL/s, $b = 0.15 t^{1/14}$ cm, and (left to right) $\sigma = 1.337, 0.925, 0.409,$ and 0.331 g/s². For all simulations, $\mu = 1/12$ g/cm·s.

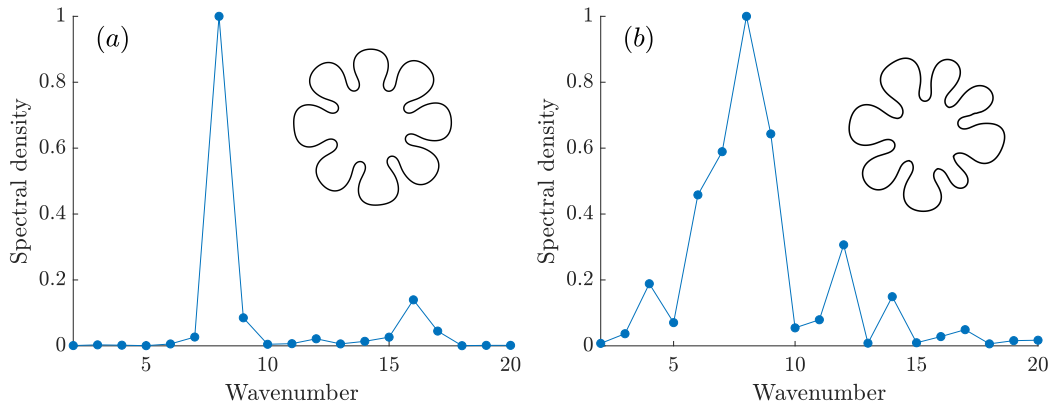


Figure 9: Normalised spectra of two different solutions to (1)-(6). For (a) $Q = 1.2$ mL/s, $b = 0.2048t^{-1/7}$ cm, $\mu = 1/12$ g/cm·s, and $\sigma = 0.1255$ g/s². For (b), $Q = 1.2t^{-1/6}$ mL/s, $b = 0.15t^{1/14}$ cm, $\mu = 1/12$ g/cm·s, and $\sigma = 0.4088$ g/s². Both of these parameter combinations give $J = 242$.

is a dimensionless control parameter. [26] showed using numerical simulations that when $\alpha_Q = -1/3$ and $\alpha_b = 0$, the interface will tend to N -fold symmetric shapes as time increases. Furthermore, the case where $\alpha_Q = 0$ and $\alpha_b = 1/7$ has been investigated experimentally by [47], who were able to produce interfaces with different numbers of non-splitting fingers. To date however, configurations where both $\alpha_Q \neq 0$ and $\alpha_b \neq 0$ have not been considered either experimentally or numerically. In this section, we perform nonlinear numerical simulations to determine whether imposing a time-dependent gap thickness and/or injection rate can be used to control the number of fingers which develop. If so, we wish to determine whether (20) is an accurate predictor of the number of fingers.

To better understand the influence of a time-dependent gap, we perform linear stability analysis on the circular solution to (1)-(6). We can show that

$$\frac{\dot{\gamma}_n}{\gamma_n} = \frac{n-1}{s_0^2} \left(\frac{Q}{2\pi b} - \frac{n(n+1)b^2\sigma}{12\mu s_0} \right) - \frac{(n+1)}{2bs_0} \frac{db}{dt}, \quad (21)$$

and the most unstable mode of perturbation

$$n_{\max} = \sqrt{\frac{1}{3} \left(\frac{Qs_0}{2b^3\pi\sigma} + 1 - \frac{s_0}{2b^3\sigma} \frac{db}{dt} \right)}. \quad (22)$$

By setting $db/dt = 0$, (21) and (22) reduce to (9) and (10). We can infer from (21) that increasing the gap between the plates, $db/dt > 0$, contributes a negative offset to the $\dot{\gamma}_n/\gamma_n$, resulting in a stabilising effect. By considering $Q = Q_1 t^{\alpha_Q}$ and $b = b_1 t^{\alpha_b}$, it can be shown that when $s_0(t) \gg s_0(0)$ and $|db/dt| \ll 0$, n_{\max} reduces to k . This suggests that when the bubble is sufficiently large, the most unstable mode according to linear stability analysis is constant, and as such, the interface will develop a constant number of fingers.

To illustrate the effect of choosing $Q \sim t^{\alpha_Q}$ and $b \sim t^{\alpha_b}$, we compute the numerical solution of (1)-(6) for different values of α_Q , α_b , and J , shown in figure 8. This figure also shows experimental results from [47] who considered $\alpha_Q = 0$ and $\alpha_b = 1/7$. Simulations are performed by considering a circular interface of radius 1 cm perturbed by modes 2 to 20 with uniformly random phases. The interface is evolved until its mean radius is 10 cm, which is approximately the same size in the experiments performed by [47] when the experiment is concluded. For each combination of α_Q and α_b considered, the interface develops non-splitting fingers, which increase in number as J increases. While the interface develops a constant number of fingers as it expands, generally bubbles do not develop clean N -fold symmetry. To illustrate this, we compute the spectral density of two different interfaces, both of which develop 8 fingers. Figure 9(a) shows the density of an interface with approximately 8-fold symmetry. The most prevalent component of this interface is the 8th mode,

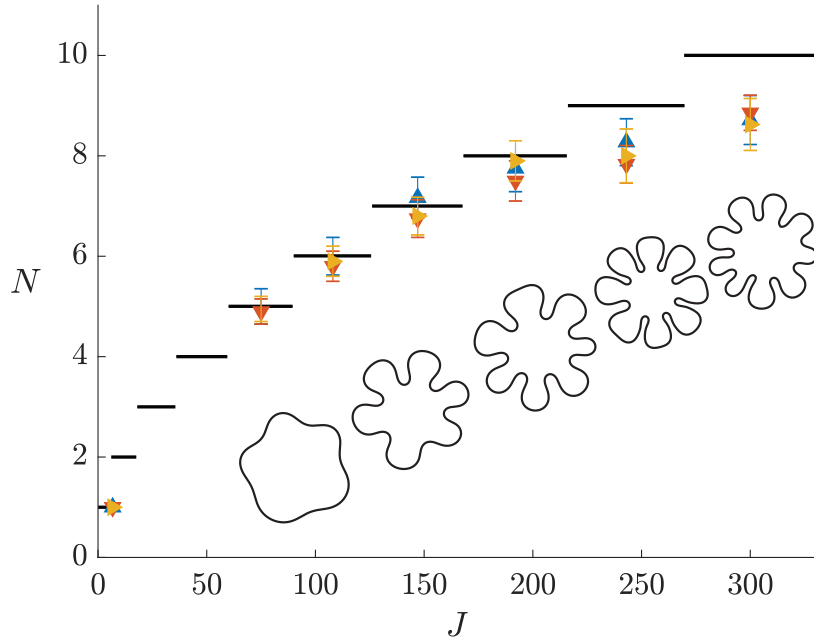


Figure 10: Average number of fingers, N , that develop as a function of the control parameter J . Injection rate and plate gap thickness are of the form $Q \sim t^{\alpha_Q}$ and $b \sim t^{\alpha_b}$ with: $\alpha_Q = -1/3$ and $\alpha_b = 0$ (\blacktriangle , blue); $\alpha_Q = 0$ and $\alpha_b = 1/7$ (\blacktriangledown , red); and $\alpha_Q = -1/6$ and $\alpha_b = 1/14$ (\blacktriangleright , yellow). Parameters used are same as figure 8. The horizontal (black) lines denote the most unstable mode of perturbation approximated from linear stability analysis by (20) rounded to the nearest integer. Inserts are examples of numerical simulations for different values of J .

and the amplitudes of all other modes, apart from the harmonic mode 16, are not significant. For a non-symmetric bubble, shown in figure 9(b), again the most prevalent contribution is from the 8th mode. However there are also significant contributions from modes 6, 7, and 9. This suggests that while a constant number of non-splitting fingers develop, nonlinear interactions between modes of perturbations still influence the evolution of the interface over the duration of the simulation.

To understand the relationship between the control parameter, J , and the morphology of the interface, we perform a series of numerical simulations for various combinations of α_Q and α_b . For each value of J considered, 10 simulations are performed, and the number of fingers at $t = t_f$ are averaged. Figure 10 shows the average number fingers as a function of J compared to the most unstable mode of perturbation according to linear stability analysis rounded to the nearest integer. The average number of fingers that develop is consistent for each combination of α_Q and α_b over the range of J values considered. On the other hand, for larger values of J , the number of fingers observed from the numerical simulations is less than number predicted by linear stability analysis. We discuss this discrepancy in §5.2.

5.2 Discussion

In this section, we have performed nonlinear simulations to determine whether imposing a time-dependent injection rate and/or plate gap can be used to control the number of fingers which develop. For each of the configurations considered, we have been able to produce interfaces which have 5 to 9 non-splitting fingers, as well as stable interfaces, i.e. 1 finger. Furthermore, we have shown that over the range of J values considered, the number of fingers observed from these simulations are in reasonable agreement with the number predicted by linear stability analysis.

While linear stability analysis provides a reasonable description of the behaviour of the interface, the nonlinear simulations presented in this section give further insight into the evolution of the interface. Specifically, while our simulations show that solutions to (1)-(6) can develop non-splitting

fingers, these interfaces generally do not develop N -fold symmetry. This is consistent with the experimental results of [24] and [47], who show that slight variations in the initial shape of the bubble can lead to variations in the width and length of the non-splitting fingers. Furthermore, for larger values of J , the number of fingers observed from simulations diverge from the theoretical prediction. A possible explanation for both of these discrepancies is that the simulations were not performed over a sufficiently long time period. Simulations presented in this section were performed using a domain size similar to that of a typical Hele-Shaw cell. It was shown numerically by [26] that when $Q \sim t^{-1/3}$, the interface develops N -fold symmetry independent of the initial condition. However, these simulations were performed on a domain significantly larger than typical Hele-Shaw cells, and are infeasible to reproduce experimentally.

6 Summary and future work

We have conducted a numerical investigation into determining how manipulating the geometry of the classic Hele-Shaw cell experiment can be used to control viscous fingering patterns. By utilising a numerical scheme based on the level set method, we have been able to compute fully nonlinear numerical solutions both when the gap between the plates is spatially and time-dependent. We have shown that our numerical solutions of (1)-(6) compare well with a variety of experimental results for different injection rates and plate configurations. Furthermore, we have been able to determine relationships between these manipulations and their influence on interfacial instabilities which extends beyond the limitations of linear stability analysis.

In §4, we demonstrated that imposing time-dependent injection rates and/or tapering the gap between the plates in the direction of flow can be used to minimise the development of viscous fingers when a fixed amount of the inviscid fluid is injected over a finite time period. In particular, we showed that tapering plate gap while imposing a time-dependent injection rate, determined using techniques from optimal control theory, results in a significant reduction in the development of instabilities. While tapering the plates suppresses viscous fingering, it was observed that numerous short fingers developed when $t_f - f \ll 1$ for both constant and time-dependent injection rates. A potential reason for this is that tapering the plates results in a reduction of the growth of perturbations for early time in exchange for faster growing perturbations as time increases. Future work could be undertaken to determine whether this occurrence could be avoided or reduced. A potential strategy could be to consider nonlinear tapering such that $\alpha \rightarrow \alpha(r)$ or different time-dependent injection rates which act to suppress the growth of instabilities as $t \rightarrow t_f$.

In §5, we provided numerical evidence indicating that imposing a time-dependent injection rate and plate gap thickness of the forms $Q \sim t^{\alpha_Q}$ and $b \sim t^{\alpha_b}$ can be used to produce bubbles with non-splitting fingers. While our results are in reasonable agreement with predictions made from linear stability analysis, we observed several discrepancies. Namely, we observed that bubbles generally did not develop clean N -fold symmetry, and that the number of fingers which developed in the numerical simulations were not consistent with theoretical predictions for larger values of J . As discussed in §5.2, a possible explanation for this discrepancy is that simulations were not run for a sufficiently long time. Numerical simulations performed by [26] who considered $\alpha_Q = -1/3$ and $\alpha_b = 0$ indicate that bubbles will develop N -fold symmetry as time becomes large. In this article, simulations presented were performed on a domain similar in size to experiments [47]. However, it may be of interest to perform long time simulations for configurations where $\alpha_b \neq 0$ to determine whether results would better match theoretical predictions. With an appropriate rescaling of (1)-(6), the numerical scheme presented in §A can be adjusted to perform simulations on a time scale much longer than that considered in this paper. Furthermore, it has been shown that self-similar solutions exist to the Hele-Shaw problem in wedge geometry when the plates are stationary and $Q \sim t^{-1/3}$ [4, 12]. Performing similar analysis when $db/dt \neq 0$ may provide further insight into the long term behaviour of the non-splitting fingers presented in §5.

Acknowledgements

The authors acknowledge the support of the Australian Research Council via the Discovery Project DP140100933, as well as the computational resources provided by the High Performance

Computing and Research Support Group at QUT.

References

- [1] AL-HOUSSEINY, T. T., CHRISTOV, I. C., AND STONE, H. A. 2013 Two-phase fluid displacement and interfacial instabilities under elastic membranes. *Phys. Rev. Lett.*, **111**, 034502.
- [2] AL-HOUSSEINY, T. T. AND STONE, H. A. 2013 Controlling viscous fingering in tapered Hele-Shaw cells. *Phys. Fluids*, **25**, 092102.
- [3] AL-HOUSSEINY, T. T., TSAI, P. A., AND STONE, H. A. 2012 Control of interfacial instabilities using flow geometry. *Nat. Phys.*, **8**, 747.
- [4] BEN AMAR, M., HAKIM, V., MASHAAL, M., AND COUDER, Y. 1991 Self-dilating viscous fingers in wedge-shaped Hele-Shaw cells. *Phys. Fluids A*, **3**, 1687–1690.
- [5] BEN-JACOB, E. AND GARIK, P. 1990 The formation of patterns in non-equilibrium growth. *Nature*, **343**, 523.
- [6] BEN-JACOB, E., SHMUELI, H., SHOCHET, O., AND TENENBAUM, A. 1992 Adaptive self-organization during growth of bacterial colonies. *Physica A*, **187**, 378–424.
- [7] BONGRAND, G. AND TSAI, P. A. 2018 Manipulation of viscous fingering in a radially tapered cell geometry. *Phys. Rev. E*, **97**, 061101.
- [8] BRENER, E., KESSLER, D., LEVINE, H., AND RAPPEL, W. 1990 Selection of the viscous finger in the 90° geometry. *Euro. Phys. Lett.*, **13**, 161.
- [9] CHEN, C. Y., CHEN, C. H., AND MIRANDA, J. A. 2005 Numerical study of miscible fingering in a time-dependent gap Hele-Shaw cell. *Phys. Rev. E*, **71**, 056304.
- [10] CHEN, J.-D. 1987 Radial viscous fingering patterns in Hele-Shaw cells. *Exp. Fluids*, **5**, 363–371.
- [11] CHEN, S., MERRIMAN, B., OSHER, S., AND SMERKA, P. 1997. A simple level set method for solving Stefan problems. *J. Comput. Phys.*, **135**, 8–29.
- [12] COMBESCOT, R. AND BEN AMAR, M. 1991 Selection of Saffman-Taylor fingers in the sector geometry. *Phys. Rev. Lett.*, **67**, 453.
- [13] DAI, W.-S. AND SHELLEY, M. J. 1993 A numerical study of the effect of surface tension and noise on an expanding Hele-Shaw bubble. *Phys. Fluids A*, **5**, 2131–2146.
- [14] DEGREGORIA, A. J. AND SCHWARTZ, L. W. 1986 A boundary-integral method for two-phase displacement in Hele-Shaw cells. *J. Fluid Mech.*, **164**, 383–400.
- [15] DIAS, E. O., ALVAREZ-LACALLE, E., CARVALHO, M. S., AND MIRANDA, J. A. 2012 Minimization of viscous fluid fingering: a variational scheme for optimal flow rates. *Phys. Rev. Lett.*, **109**, 144502.
- [16] DIAS, E. O. AND MIRANDA, J. 2010 Control of radial fingering patterns: A weakly nonlinear approach. *Phys. Rev. E*, **81**, 016312.
- [17] DIAS, E. O. AND MIRANDA, J. A. 2013 Taper-induced control of viscous fingering in variable-gap Hele-Shaw flows. *Phys. Rev. E*, **87**, 053015.
- [18] DIAS, E. O., PARISIO, F., AND MIRANDA, J. A. 2010 Suppression of viscous fluid fingering: A piecewise-constant injection process. *Phys. Rev. E*, **82**, 067301.
- [19] ENRIGHT, D., FEDKIW, R., FERZIGER, J., AND MITCHELL, I. 2002 A hybrid particle level set method for improved interface capturing. *J. Comput. Phys.*, **183**, 83–116.
- [20] FAST, P. AND SHELLEY, M. J. 2004 A moving overset grid method for interface dynamics applied to non-Newtonian Hele-Shaw flow. *J. Comput. Phys.*, **195**, 117–142.
- [21] HOMSY, G. M. 1987 Viscous fingering in porous media. *Ann. Rev. Fluid Mech.*, **19**, 271–311.
- [22] HOU, T. Y., LI, Z., OSHER, S., AND ZHAO, H. 1997 A hybrid method for moving interface problems with application to the Hele-Shaw flow. *J. Comput. Phys.*, **134**, 236–252.
- [23] JACKSON, S. J., POWER, H., GIDDINGS, D., AND STEVENS, D. 2017 The stability of immiscible viscous fingering in Hele-Shaw cells with spatially varying permeability. *Comput. Methods Appl. Mech. Eng.*, **320**, 606–632.

- [24] LESHCHINER, A., THRASHER, M., MINEEV-WEINSTEIN, M. B., AND SWINNEY, H. L. 2010 Harmonic moment dynamics in Laplacian growth. *Phys. Rev. E*, **81**, 016206.
- [25] LI, S., LOWENGRUB, J., LEO, P. H., AND CRISTINI, V. 2004 Nonlinear theory of self-similar crystal growth and melting. *J. Cryst. Growth*, **267**, 703–713.
- [26] LI, S., LOWENGRUB, J. S., FONTANA, J., AND PALFFY-MUHORAY, P. 2009 Control of viscous fingering patterns in a radial Hele-Shaw cell. *Phys. Rev. Lett.*, **102**, 174501.
- [27] LIANG, S. 1986 Random-walk simulations of flow in Hele Shaw cells. *Phys. Rev. A*, **33**, 2663.
- [28] LINDNER, A., DERKS, D., AND SHELLEY, M. J. 2005 Stretch flow of thin layers of Newtonian liquids: Fingering patterns and lifting forces. *Phys. Fluids*, **17**, 072107.
- [29] LINS, T. F. AND AZAIEZ, J. 2017 Resonance-like dynamics in radial cyclic injection flows of immiscible fluids in homogeneous porous media. *J. Fluid Mech.*, **819**, 713–729.
- [30] LISTER, J. R., PENG, G. G., AND NEUFELD, J. A. 2013 Viscous control of peeling an elastic sheet by bending and pulling. *Phys. Rev. Lett.*, **111**, 154501.
- [31] LU, D., MUNICCHI, F., AND CHRISTOV, I. C. 2018 Computational analysis of interfacial instability in angled Hele-Shaw cells. *arXiv preprint 1811.06960*.
- [32] MIRZADEH, M. AND BAZANT, M. Z. 2017 Electrokinetic control of viscous fingering. *Phys. Rev. Lett.*, **119**, 174501.
- [33] MORONEY, T. J., LUSMORE, D. R., MCCUE, S. W., AND MCELWAIN, S. (2017). Extending fields in a level set method by solving a biharmonic equation. *J. Comput. Phys.*, **343**, 170–185.
- [34] MULLINS, W. W. AND SEKERKA, R. 1988 Stability of a planar interface during solidification of a dilute binary alloy. In *Dynamics of Curved Fronts*, pages 345–352. Elsevier.
- [35] NASE, J., DERKS, D., AND LINDNER, A. 2011 Dynamic evolution of fingering patterns in a lifted Hele-Shaw cell. *Phys. Fluids*, **23**, 123101.
- [36] OSHER, S. AND SETHIAN, J. A. 1988 Fronts propagating with curvature-dependent speed: algorithms based on Hamilton-Jacobi formulations. *J. Comput. Phys.*, **79**, 12–49.
- [37] PATERSON, L. 1981 Radial fingering in a Hele Shaw cell. *J. Fluid Mech.*, **113**, 513–529.
- [38] PIHLER-PUZOVIC, D., ILLIEN, P., HEIL, M., AND JUEL, A. 2012 Suppression of complex fingerlike patterns at the interface between air and a viscous fluid by elastic membranes. *Phys. Rev. Lett.*, **108**, 074502.
- [39] PIHLER-PUZOVIC, D., JUEL, A., AND HEIL, M. 2014 The interaction between viscous fingering and wrinkling in elastic-walled Hele-Shaw cells. *Phys. Fluids*, **26**, 022102.
- [40] PIHLER-PUZOVIC, D., PENG, G. G., LISTER, J. R., HEIL, M., AND JUEL, A. 2018 Viscous fingering in a radial elastic-walled Hele-Shaw cell. *J. Fluid Mech.*, **849**, 163–191.
- [41] PIHLER-PUZOVIC, D., PÉRILLAT, R., RUSSELL, M., JUEL, A., AND HEIL, M. 2013 Modelling the suppression of viscous fingering in elastic-walled Hele-Shaw cells. *J. Fluid Mech.*, **731**, 162–183.
- [42] RABBANI, H. S., OR, D., LIU, Y., LAI, C.-Y., LU, N. B., DATTA, S. S., STONE, H. A., AND SHOKRI, N. 2018 Suppressing viscous fingering in structured porous media. *Proc. Natl. Acad. Sci.*, page 201800729.
- [43] SAFFMAN, P. G. AND TAYLOR, G. I. 1958 The penetration of a fluid into a porous medium or Hele-Shaw cell containing a more viscous liquid. *Proc. R. Soc. Lond. A*, **245**, 312–329.
- [44] SHELLEY, M. J., TIAN, F., AND WLODARSKI, K. 1997 Hele-Shaw flow and pattern formation in a time-dependent gap. *Nonlinearity*, **10**, 1471.
- [45] STONE, H. A. 2017 Seeking simplicity for the understanding of multiphase flows. *Phys. Rev. Fluids*, **2**, 100507.
- [46] WITTEN, T. A. AND SANDER, L. M. 1983 Diffusion-limited aggregation. *Phys. Rev. B*, **27**, 5686.
- [47] ZHENG, Z., KIM, H., AND STONE, H. A. 2015 Controlling viscous fingering using time-dependent strategies. *Phys. Rev. Lett.*, **115**, 174501.

A Numerical scheme

A.1 The level set method

To implement the level set method, a level set function, $\phi(\mathbf{x}, t)$, is constructed as a signed distance function whose zero level set describes the location of the interface between the viscous and inviscid fluid regions, and

$$\begin{aligned}\phi &> 0 && \text{if } \mathbf{x} \in \mathbb{R}^2 \setminus \Omega(t), \\ \phi &< 0 && \text{if } \mathbf{x} \in \Omega(t).\end{aligned}$$

If the interface has a normal speed V_n , then we wish to construct a function, F , such that $F = V_n$ on the interface and is continuous over the entire computational domain. Thus ϕ satisfies the level set equation

$$\frac{\partial \phi}{\partial t} + F|\nabla \phi| = 0. \quad (23)$$

We approximate the spatial derivatives in (23) using an second order essentially non-oscillatory scheme, and the time derivative using second order Runge-Kutta. We choose a time step size of $\Delta t = 0.25 \times \Delta x / \max |F|$ to ensure stability. Furthermore, to maintain ϕ as a signed distance function, re-initialisation is periodically performed by solving

$$\frac{\partial \phi}{\partial \tau} + S(\phi)(|\nabla \phi| - 1) = 0,$$

to steady state where

$$S(\phi) = \frac{\phi}{\sqrt{\phi^2 + \Delta x^2}},$$

and τ is a pseudo time variable.

A major limitation of the level set method is that solutions can suffer from volume loss (or gain). To alleviate this problem, we implement the particle level set method, which combines the Eulerian level set method with a marker particle based Lagrangian approach. The particle level set method, first proposed by [19], extends the traditional level set method by placing massless marker particles around the interface. These particles are advected using the same velocity field as the level set function. As the particles do not suffer from mass loss, the level set function can be corrected if the particles are found to incorrectly cross the interface. We refer the reader to [19] for details on how to implement the particle level set method, as well as examples illustrating its effectiveness.

A.2 Solving for F

By defining $\mathbf{n} = \nabla \phi / |\nabla \phi|$ as the outward facing normal of the interface, then we have the expression for F

$$F = -\frac{b^2}{12\mu} \frac{\nabla p \cdot \nabla \phi}{|\nabla \phi|} \quad \mathbf{x} \notin \Omega(t).$$

This satisfies (5) on the interface, and provides a continuous expression for F in the viscous fluid region. However, to solve (23) we require an expression for F over the entire computational domain. [33] proposed that the speed function can be extended into the inviscid fluid region by solving the biharmonic equation

$$\nabla^4 F = 0 \quad \mathbf{x} \in \Omega(t). \quad (24)$$

By solving (24), this ensures that $F = V_n$ on the interface and gives a continuous expression for F away from the interface. The sign of ϕ is used to determine nodes inside the interface that need to be included in the biharmonic stencil. As such, the location of the interface does not need to be known explicitly, similar to the level set method itself. We note that this velocity extension process is a variant of a thin plate spline in two dimensions. We refer the reader to [33] for further details.

A.3 Solving for pressure

To evaluate the speed function F , we must first compute the pressure field. We consider (1)-(6) in polar coordinates with $p = p(r, \theta, t)$ and the location of the interface is given by $r = s(\theta, t)$. Thus (3) becomes

$$\frac{1}{r} \frac{\partial}{\partial r} \left(\frac{rb^3}{12\mu} \frac{\partial p}{\partial r} \right) + \frac{1}{r^2} \frac{\partial}{\partial \theta} \left(\frac{b^3}{12\mu} \frac{\partial p}{\partial \theta} \right) = \frac{\partial b}{\partial t} \quad r > s(\theta, t). \quad (25)$$

In order to solve for the pressure at nodes that are not adjacent to the interface, we discretise (25) using a standard central finite difference scheme. Denoting $\beta = rb^3/12\mu$, the r -derivatives in (25) are approximated via

$$\frac{1}{r} \frac{\partial}{\partial r} \left(\beta \frac{\partial p}{\partial r} \right) \rightarrow \frac{1}{r_{i,j} \Delta r} \left(\beta_{i+1/2,j} \frac{p_{i+1,j} - p_{i,j}}{\Delta r} - \beta_{i-1/2,j} \frac{p_{i,j} - p_{i-1,j}}{\Delta r} \right),$$

where $\beta_{i+1/2,j} = (\beta_{i+1,j} + \beta_{i,j})/2$ and $\beta_{i-1/2,j} = (\beta_{i-1,j} + \beta_{i,j})/2$. The derivatives in the θ -direction are discretised in a similar fashion.

Special care must be taken when solving for nodes adjacent to the interface. Suppose that the interface is located at $r = r_I$ where $r_{i,j} < r_I < r_{i+1,j}$. When discretising (25), we can no longer incorporate $p_{i+1,j}$ into our finite difference stencil as it is not in the domain $\mathbf{x} \in \mathbb{R}^2 \setminus \Omega(t)$. Instead, we define a ghost node at r_I whose value is p_I . By noting that ϕ is a signed distance function, the distance between $r_{i,j}$ and r_I is approximated via

$$h = \Delta r \left| \frac{\phi_{i,j}}{\phi_{i+1,j} - \phi_{i,j}} \right|.$$

As per [11], our finite difference stencil becomes

$$\begin{aligned} \frac{1}{r} \frac{\partial}{\partial r} \left(\beta \frac{\partial p}{\partial r} \right) &\rightarrow \frac{2}{r_{i,j}(\Delta r + h)} \left(-\hat{\beta}_{i+1/2,j} \frac{p_{i,j}}{h} - \beta_{i-1/2,j} \frac{p_{i,j} - p_{i-1,j}}{\Delta r} \right) \\ &\quad + \underbrace{\frac{2}{r_{i,j}h(\Delta r + h)} \hat{\beta}_{i+1/2,j} p_I}_{\text{non-homog.}}. \end{aligned}$$

Here $\hat{\beta}_{i,j+1/2} = (\beta_{i,j} + \beta_I)/2$ where β_I is the value of β on the interface, and is computed via linear interpolation using $\beta_{i,j}$ and $\beta_{i,j+1}$. When the node and interface are sufficiently close together such that $h < \Delta r^2$, we set $p_{i,j} = p_I$. The value of p_I is computed from the dynamic boundary condition (4), where the curvature of the interface is $\kappa = \nabla \cdot \mathbf{n}$.

A.3.1 Far-field boundary condition

To incorporate the far-field boundary condition (5) into our finite difference stencil, we utilise a Dirichlet to Neumann map. This is implemented by imposing an artificial circular boundary at $r = R$ such that $R > s(\theta, t)$. By only considering the region in domain $r \geq R$, we seek a solution to (3) of the form

$$p(r, \theta, t) = A_0 + \frac{Q}{2\pi} \log r + \frac{r^2}{4} \frac{\partial b}{\partial t} + \sum_{n=1}^{\infty} r^{-n} (A_n \cos n\theta + B_n \sin n\theta). \quad (26)$$

where A_0 , A_n , and B_n are unknown. Considering the value of pressure on the artificial boundary, suppose that $p(R, \theta, t)$ can be represented as a Fourier series

$$p(R, \theta, t) = a_0 + \sum_{n=1}^{\infty} a_n \cos n\theta + b_n \sin n\theta, \quad (27)$$

where

$$\begin{aligned} a_0 &= \frac{1}{2\pi} \int_0^{2\pi} p(R, \theta, t) \, d\theta, \\ a_n &= \frac{1}{\pi} \int_0^{2\pi} p(R, \theta, t) \cos n\theta \, d\theta, \\ b_n &= \frac{1}{\pi} \int_0^{2\pi} p(R, \theta, t) \sin n\theta \, d\theta. \end{aligned}$$

By equating (27) with (26) evaluated at $r = R$, we find that $A_0 = a_0 - Q \log R - \dot{b}R^2/4$, $A_n = R^n a_n$ and $B_n = R^n b_n$.

By differentiating our expression for p with respect to r and evaluate it at $r = R$ to give

$$\begin{aligned} \left. \frac{\partial p}{\partial r} \right|_{r=R} &= \frac{Q}{2\pi R} + \frac{R}{2} \frac{\partial b}{\partial t} - \sum_{n=1}^{\infty} \frac{n}{\pi R} (a_n \cos n\theta + b_n \sin n\theta), \\ \frac{p_{i+1,j} - p_{i,j}}{\Delta r} &\approx \frac{Q}{2\pi R} + \frac{R}{2} \frac{\partial b}{\partial t} - \frac{\Delta\theta}{R\pi} \sum_{j=1}^m (w_{ij} + v_{ij}) p_{i,j}, \end{aligned}$$

where

$$w_{ij} = \sum_{n=1}^{\infty} n \cos n\theta_j \cos n\theta_i, \quad v_{ij} = \sum_{n=1}^{\infty} n \sin n\theta_j \sin n\theta_i.$$

To incorporate our expression for $\partial p/\partial r$ at $r = R$ into our finite difference stencil,

$$\begin{aligned} \frac{1}{r} \frac{\partial}{\partial r} \left(\beta \frac{\partial p}{\partial r} \right) &\rightarrow - \frac{(2R + \Delta r)\Delta\theta}{\pi R^2 \Delta r} \left(\sum_{j=1}^m (w_{ij} + v_{ij}) p_{i,j} \right) \\ &\quad - \beta_{i-1/2,j} \frac{p_{i,j} - p_{i-1,j}}{R\Delta r^2} + \frac{2R + \Delta r}{2\Delta r R} \left(\frac{Q}{2\pi R} - \frac{\partial b}{\partial t} \frac{R}{2} \right), \end{aligned}$$

recalling $\beta = rb^3/12\mu$. We note that the finite difference stencil for the derivatives in the θ -direction is not changed.